Covalent-bond-linked monolayer fullerene network as a spin sponge for spin-triplet O_2 activation and CO oxidation

Haoyong Suo,[1] Manfu Li,[1] Guang Yang,[1] Yuxin Du,[1] Xingju Zhao,[1,2] Xiaoyan Ren,[1,*] and Shunfang Li[1,2,†]
[1]*Key Laboratory of Material Physics, Ministry of Education, School of Physics and Microelectronics, Zhengzhou University, Zhengzhou 450001, China*
[2]*Institute of Quantum Materials and Physics, Henan Academy of Sciences, Zhengzhou 450046, China*

(Received 19 June 2024; accepted 22 August 2024; published 5 September 2024)

Recently, a novel class of 2D carbon material, covalent-bond-linked monolayer C_{60} networks with quasi-hexagonal phase (qHP-C_{60}) was experimentally fabricated [Hou *et al.*, Nature (London) **606**, 507 (2022)]. Here, using first-principles calculations, we predict that such a two-dimensional network serves as an ideal platform in stabilizing transition metals (TM: Mn, Fe, Co, and Ni) into dispersive single atoms, exhibiting remarkable efficiency for spin-triplet O_2 activation and CO oxidation with low reaction barriers ($0.3 \sim 0.5$ eV). First, the two-dimensional qHP-C_{60} network acts as an electronic reservoir responsible for charge transfer to the antibonding orbital of O_2. Second, and important, it functions as a spin sponge in accommodation of the reduced spin magnetic moment from O_2 molecule, facilitating its spin triplet-to-singlet transition in the framework of Wigner's spin conservation rule. Delicate quantitative calculations demonstrate that the spin component contributes approximately twice as significantly as that of pure charge transfer in reducing the activation barrier for CO oxidation.

DOI: 10.1103/PhysRevB.110.125405

I. INTRODUCTION

Carbon, as one of the most abundant and fundamental elements, exhibits versatility in forming various allotropes with a broad range of fascinating properties [1]. The diverse bonding states of carbon, encompassing sp, sp^2, and sp^3 hybridizations, give rise to zero-dimensional (0D), one-dimensional (1D), two-dimensional (2D), and three-dimensional (3D) carbon structures, such as fullerene [2], carbon nanotubes [3], graphene [4], and diamond [5]. These materials, respectively, exhibit conspicuous characteristics and play a leading role in advancing modern science and technology [2–7]. Particularly noteworthy is the 0D cagelike fullerene C_{60} [2], as also termed superatom [8] with extraordinary stability, has attracted tremendous interest in the realm of single-molecule semiconductor devices, such as polymer solar cells [9,10], transistors, and functional transport devices [11–14]. Moreover, C_{60} presents attractive prospects in fullerene chemistry [15], such as photocatalysis [16] and electrocatalysis [17], owing to its large surface area, abundant surface-active sites, and distinctive electron acceptor characteristics [18–20]. Specifically, prior research has reported that C_{60} can function as an electron buffer or transmitter, accelerating intermolecular electron transfer processes and creating extremely active surfaces for catalysis [20–24].

Recently, a novel class of single-crystal 2D carbon material, specifically monolayer C_{60} networks, was experimentally fabricated utilizing an interlayer bond-cleavage strategy [25–27]. Note that these monolayer C_{60} networks are linked by covalent bonds, which integrate both the merits of 0D superatoms and 2D materials, demonstrating unique physical and chemical characteristics such as anisotropic optical properties [25,28] and exceptional photocatalytic performance in water splitting [29–31]. Nevertheless, the appealing application of covalent-bond-linked 2D-C_{60} network-based materials in semiconducting nanodevices and fullerene chemistry still faces several critical challenges. One notable challenge involves achieving precise control over the interfacial interactions between 2D-C_{60} network and the other materials, including metals, at the single-atomic scale. This precision is essential in comprehending the atomistic mechanism of the charge transfer and associated physiochemical processes in C_{60}-based frameworks. As the dimensionality reduces to the single-atomic scale, enhanced magnetism becomes a common observation in various transitional metals [32–34]. Consequently, for TM-C_{60}-network interactions, a comprehensive consideration of both charge transfer and spin accommodation is imperative, particularly in the design of C_{60}-based spintronic devices and catalytic platforms. Especially, in catalytic applications, the relevance of Wigner's spin selection rule to various chemical processes [35–37] should be definitely acknowledged. However, up to date, to the best of our knowledge, the interactions between TM single atoms and 2D-C_{60} network [25–27] are still unclear. Fundamental questions concerning the charge transfer and spin interactions between TM single atoms and 2D-C_{60} network remain absent. Moreover, although recent research reveals that spin states are qualitatively crucial in determining the overall catalysis of various catalytic reactive sites in single-atomic scale [37–40], identifying its quantitative importance

*Contact author: renxyan@zzu.edu.cn
†Contact author: sflizzu@zzu.edu.cn

in a given chemical process represents a compelling yet challenging task.

Here, based on state-of-the-art first-principles calculations, taking the recently fabricated quasihexagonal phase (qHP-C_{60}) [25] as a typical example, we identified that such covalent-bond-linked 2D-C_{60} network serves as an ideal platform for stabilizing magnetic 3d-TM (TM = Mn, Fe, Co, and Ni) as dispersive single atoms within the pores formed between C_{60} cages. Remarkably, these TM_1@qHP-C_{60} single-atom catalyst (SAC) systems exhibit highly efficient catalytic performance for spin-triplet O_2 activation and CO oxidation, overcoming fairly low energy barriers ($0.36 \sim 0.51$ eV). Strikingly, the supporting qHP-C_{60} not only functions as an electronic reservoir, dominating the charge transfer for both electron acceptor and donor, but also serves as a two-dimensional spin sponge, playing a leading rule in the spin selection of the catalytic processes. Importantly, through delicate comparisons, we demonstrate that quantitatively, the spin component plays a vital role approximately twice as significant as that of pure charge transfer in reducing the activation barrier for CO oxidation. Furthermore, we establish a well-defined linear-like scaling dependence between the contributions of charge–spin from the qHP-C_{60} and the catalysis of the TM_1@qHP-C_{60} complexes.

This paper is organized as follows. The methods and details of first-principles calculations are introduced in Sec. II. The results and discussion of the electronic and catalytic properties are presented in Sec. III. Finally, we present a brief summary in Sec. IV.

II. METHODS

Our spin-polarized density-functional theory (DFT) calculations [41] were performed using the Vienna *Ab initio* Simulation Package (VASP) [42,43] with the projector augmented-wave [44,45] method. For the exchange-correlation energy, we employed the generalized-gradient approximation functional of revised Perdew-Burke-Ernzerhof [46]. The electronic wave functions were expanded in a plane-wave basis with an energy cutoff of 500 eV, and the k-space integration was performed with a $2\times3\times1$ Monkhorst-Pack k-point mesh in the Brillouin zone. The 2D qHP-C_{60} was simulated by a periodic slab model with a vacuum thickness of ~18 Å. Strong Coulomb interactions of 3d electron of transition metal were described with DFT+U [47] approach, with $U_{\mathrm{eff}} = 3.06$, 3.29, 3.42, and 3.40 eV for TM = Mn, Fe, Co, and Ni, respectively [48]. In addition, the zero-damping DFT-D3 method [49,50] was adopted in describing van der Waals interactions. The atomic positions were optimized by a conjugate gradient algorithm until the forces in all directions were less than 0.02 eV/Å and the convergence criterion for electronic step was within 10^{-4} eV. The optimized lattice constants of qHP-C_{60} were $a = 15.94$ Å and $b = 9.17$Å, in close agreement with previous report [25]. The adsorption energy (E_{ads}) of O_2 (CO) molecule is defined as $E_{\mathrm{ads}} = -[E(O_2(CO)/TM_1@qHP\text{-}C_{60}) - E(TM_1@qHP\text{-}C_{60}) - E(O_2(CO))]$, where the three terms in the right-hand side of the equation represent the total energies of the optimized O_2(CO)/TM_1@qHP-C_{60} complex, TM_1@qHP-C_{60} component, and gas phase of O_2(CO) molecule, respectively. The well-recognized climbing-image nudged elastic band (CI-NEB) method [51,52] was used to identify the minimum-energy paths (MEPs) and transition state.

III. RESULTS AND DISCUSSION

First, we provide a concise overview of the geometric structure of the covalent-bond-linked 2D qHP-C_{60} network, as shown in Fig. 1(a), where each C_{60} is covalently linked with six adjacent C_{60} cages, with four C–C single bonds along the diagonal lines of the rectangular unit cell and two [2+2] cycloaddition bonds in the vertical direction [25]. Particularly, the unit cell is featured with four symmetric and substantial pores established among the adjacent C_{60} cages, each with a diameter of approximately 5.32 Å, indicating its significant advantages in trapping the adsorbed TM atoms. Figure 1(b) presents the density of states (DOS) and band structure of the 2D qHP-C_{60} network calculated by the screened hybrid functional Heyd-Scuseria-Ernzerhof (HSE) [53], in close agreement with both the experimental and previously calculated values [25,28].

We continue to investigate the adsorption behavior of TM atoms (TM = Mn, Fe, Co, and Ni) on the 2D qHP-C_{60} network. Here, eight high-symmetry adsorption sites (including T_1, B_2, B_3, H_4, H_5, B_6, H_7, and H_8) and some low-symmetry sites are considered, as shown in Fig. 1(a) and detailed (see Sec. I of the Supplemental Material [54]). The binding energy (E_{b}) of the TM atom is calculated by $E_{\mathrm{b}} = [E(\mathrm{TM}) + E(\mathrm{qHP\text{-}C_{60}}) - E(\mathrm{TM_1@qHP\text{-}C_{60}})]$, where E(TM), E(qHP-C_{60}), and E(TM_1@qHP-C_{60}) represent the total energies of the optimized TM single atom, qHP-C_{60}, and TM_1@qHP-C_{60} complex where one TM atom is deposited on qHP-C_{60}, respectively. As illustrated (see Sec. II of the Supplemental Material, Fig. S1 [54]), extensive calculations demonstrate that all the considered TM atoms exhibit a preference of confinement at the H_7 site. The E_{b} for Mn, Fe, Co, and Ni are, respectively, calculated to be 1.48, 2.09, 2.64, and 3.19 eV, which are larger than that of a Mg single atom on the fabricated qHP-C_{60} where Mg atoms are incorporated [25]. Subsequently, taking TM = Mn as a typical example, we further examine the kinetics of the confined TM atoms. The MEP calculated by CI-NEB [51,52] reveals that the E_{bar} for a Mn single atom jumping between two neighboring H_7 sites is about 1.27 eV [see Fig. 1(c)], corresponding to a diffusion and thus nucleation rate (R) of $4.62 \times 10^{-9}\ \mathrm{s}^{-1}$, as estimated by an Arrhenius-type activation process, with the definition of $R = R_0 \exp(-E_{\mathrm{bar}}/k_{\mathrm{B}}T)$. Here, R_0, E_{bar}, k_{B}, and T correspond to the characteristic prefactor with a typical value of $10^{13}\ \mathrm{s}^{-1}$, diffusion-energy barrier, Boltzmann constant, and room temperature, respectively. Clearly, such a substantial E_{bar} effectively hinders the aggregation of Mn atoms. Furthermore, the thermodynamic stability of Mn_1@qHP-C_{60} complex is further confirmed through *ab initio* molecular dynamic simulations at 300 K (see Sec. II of the Supplemental Material, Fig. S2 [54]). Here, we also note that the thermodynamic stability of the qHP-C_{60} substrate network has been also confirmed up to about 700 K by classic molecular dynamic simulations [55]. These findings suggest that

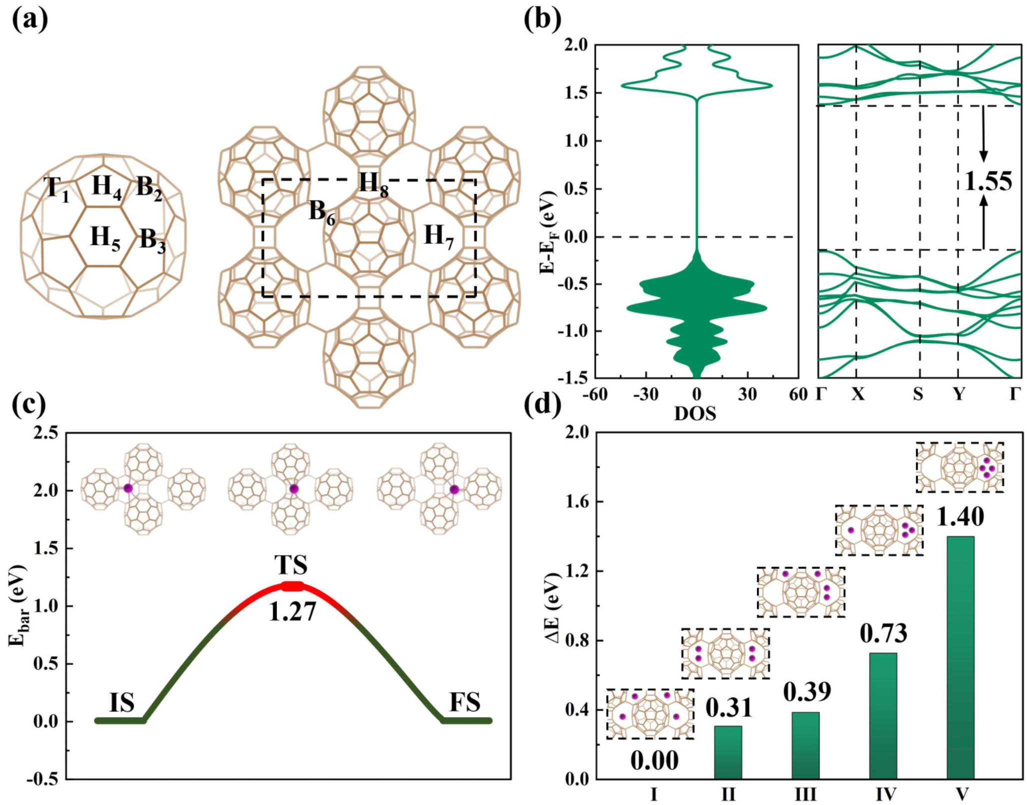

FIG. 1. (a) Structure of covalent-bond-linked 2D qHP-C_{60} monolayer, with eight high-symmetry adsorption sites being marked, i.e., T_1, B_2, B_3, H_4, H_5, B_6, H_7, and H_8. (b) Projected density of states (DOS) and band structures of 2D qHP-C_{60}. (c) Activation energy barrier (E_{bar}) in the minimum-energy path for a single Mn atom diffusion between two neighboring preferred adsorption sites (H_7) on 2D qHP-C_{60} monolayer. (d) Relative energies (ΔE) of five typical configurations for 4 Mn atoms deposited on 2D qHP-C_{60} monolayer.

the present Mn_1@qHP-C_{60} complex can be really stable far beyond room temperature.

To ascertain whether TM atoms prefer single-atomic dispersion or clustering, we expanded the coverage of the deposited TM atoms up to 4, considering the presence of 4 H_7 sites in the current system. Comprehensive calculations demonstrate that the 4 TM atoms favor a single-atomic dispersion, with each atom exclusively occupying each H_7 site, thus forming a so-called "1+1+1+1" configuration. Alternative configurations, such as clustering depicted by "2+1+1+0," "2+2+0+0," "3+1+0+0," and "4+0+0+0" motifs, are energetically unfavorable, as exemplified by the case of TM = Mn [see Fig. 1(d)] and detailed in Sec. II of the Supplemental Material, Fig. S3 [54]). Collectively, these findings convincingly prove that the present 2D qHP-C_{60} functions as an ideal harboring substrate for confining TM single atoms.

Now, we provide a concise overview of the interactions between the TM single atoms and the 2D qHP-C_{60} substrate. First, we confirm that the adsorption of a single TM atom onto the nonmagnetic 2D qHP-C_{60} monolayer is accompanied with substantial charge transfer, due to the well-known electron withdrawing characteristics of the latter [20]. Specifically, for Mn, Fe, Co, and Ni, about 1.06, 0.85, 0.71, and 0.43 $|e|$ are transferred from each TM atom to the 2D substrate, respectively, as summarized in Table S1 of Supplemental Material [54]. Correspondingly, the optimized magnetic moments (MM) of these 4 TM_1@qHP-C_{60} complexes are 3, 2, 1, and 0 μ_B, respectively. Noteworthy is that in the first three cases, ferrimagnetic couplings are identified between the deposited TM single atom and the underlying C atoms, as indicated by the local projected MM analysis. Specifically, 4.14 (−1.14), 3.02 (−1.02), and 1.99 (−0.99) μ_B are observed on Mn (qHP-C_{60}), Fe (qHP-C_{60}), and Co (qHP-C_{60}), respectively. Moreover, taking Mn as a representative example, we have also confirmed a ferromagnetic coupling between two atomically dispersed Mn atoms on the qHP-C_{60} complex simulated in the present unit cell, with the local MM and the ferrimagnetic coupling with the nearby C atoms almost unchanged, as that of Mn_1@qHP-C_{60}.

To further decipher the precise interactions between the TM single atoms and the supporting qHP-C_{60}, and the consequent impacts on practical applications, such as in the field of SAC, we investigate a prototypical important process involving O_2 activation (CO oxidation) on the present systems. This process incorporates both charge transfer [56,57] and spin-triplet to spin-singlet transition [58–60]. Note that for O_2/CO adsorptions, we have considered various initial orientations and symmetries, including the case that the O_2 molecule is close to both the TM catalytic site and carbon atoms of the qHP-C_{60} substrate. However, our calculations show that even if initially we manually place the O_2 molecule nearby the C_{60}, it will be automatically relaxed back to the TM-active site. These findings suggest that on the one hand, these TM single atoms serve as catalytic reactive sites for O_2 activation and CO oxidation; on the other hand, they may also effectively prevent the oxidation of the qHP-C_{60} substrate. The optimized

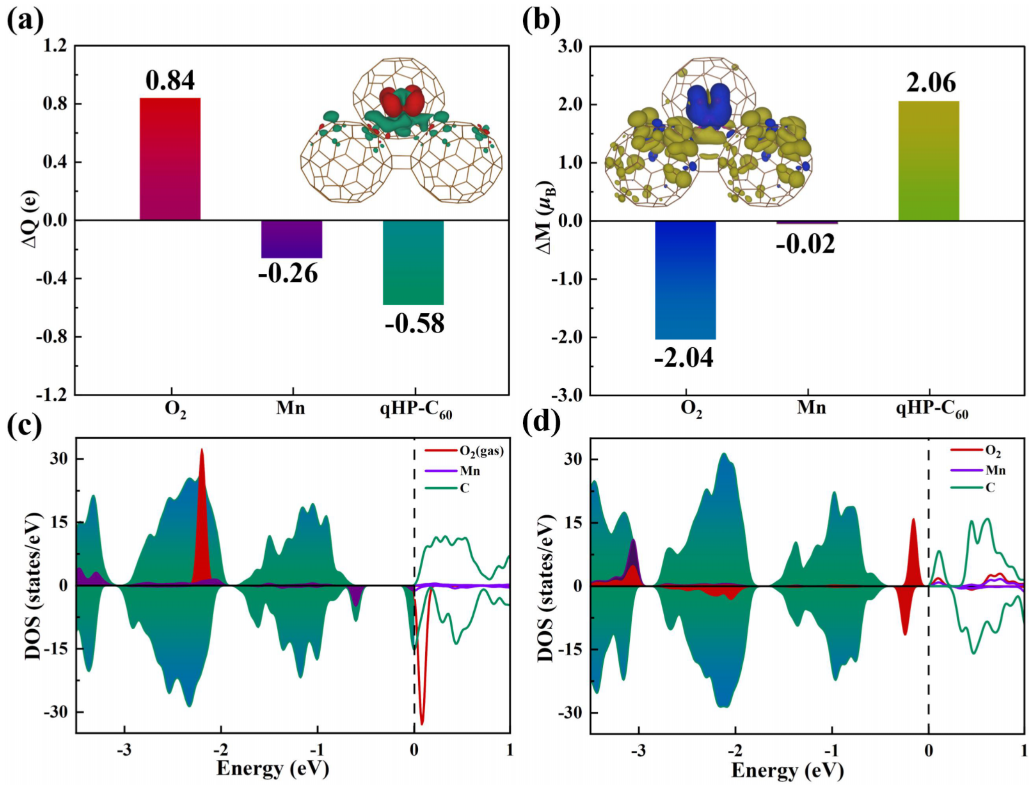

FIG. 2. Electronic structure analysis for O_2 adsorption. (a) Charge transfer ΔQ, and (b) magnetic moment changes ΔM. Here, a positive and negative ΔQ signify charge accumulation and depletion, respectively. The charge-density difference ($\Delta\rho$) and the spin-density difference (Δs) (with an isosurface value of 0.008 e/Å^3) upon O_2 adsorption on the Mn-reactive site of Mn_1@qHP-C_{60} complex is also inserted (red–yellow and green–blue isosurface represents the electron (spin) accumulation and electron (spin) depletion, respectively), where $\Delta\rho = \rho(O_2/Mn_1@qHP\text{-}C_{60})\text{-}\rho(O_2)\text{-}\rho(Mn_1@qHP\text{-}C_{60})$; the definition of Δs is similar to $\Delta\rho$. Electronic DOS of Mn_1@qHP-C_{60} for the cases of (c) before and (d) after O_2 adsorption on the Mn-reactive site.

configurations and adsorption energies (E_{ads}) of O_2 and CO on the TM reactive sites are presented in Sec. II of the Supplemental Material, Fig. S4 [54]. Our findings reveal that as the number of unoccupied d orbital decreases, from Mn(d^6), Fe(d^7), and Co(d^8), to Ni(d^9), the $E_{ads}(O_2)$ progressively decreases, with an order of 1.34, 1.09, 0.65, and 0.51 eV, respectively. In contrast, overall the E_{ads} of CO increases, from 0.64, 0.84, and 1.11, to 1.06 eV, respectively. The bond-length variations of both the adsorbed O_2 and CO are detailed in Sec. II of the Supplemental Material, Fig. S4 [54]. Note that based on extensive calculations, we confirm that the present TM single atoms (TM = Mn, Fe, Co, and Ni) prefer to adsorb on the H_7 large hollow site for both cases without and with O_2/CO adsorption.

Next, taking the Mn_1@qHP-C_{60} catalytic platform as a representative example, we explore the role of the underlying qHP-C_{60} in O_2 activation from the spin triplet-to-singlet transition. Bader charge-transfer (ΔQ) analysis demonstrates that upon O_2 adsorption on the Mn_1@qHP-C_{60}, around 0.84 $|e|$ is transferred from the latter to the former, as shown in Fig. 2(a). Nevertheless, although the O_2 molecule prefers the adsorption on Mn-reactive site, the supporting qHP-C_{60} contributes most of the charge transfer, 0.58 $|e|$. In contrast, the Mn single-atom reactive site itself donates merely 0.26 $|e|$. These findings imply that while the activation of the spin-triplet O_2 occurs on the d-block Mn single atom, the assembled p-block elemental qHP-C_{60} network functions as a crucial electronic reservoir dominating the charge donation. Note that although C_{60} is conventionally recognized as a charge acceptor in various chemical processes [23,24], here it plays a key role as a charge donor.

Furthermore, a specific spin evolution process is identified for O_2 adsorption. The total MM of the optimized O_2/Mn_1@qHP-C_{60} system is 5 μ_B (see Sec. II of the Supplemental Material, Fig. S5 [54]). That is, the spin-spin coupling between the spin-triplet O_2 molecule ($S = 1$) and the Mn_1@qHP-C_{60} complex ($S = 3/2$) follows the spin-allowed channel of "3/2 + 1 = 5/2," according to Wigner's spin selection [35–37]. This rule restricts that the total spin quantum numbers, $S(O_2/Mn_1@qHP\text{-}C_{60})$, of the spin-allowed reaction should satisfy $S(O_2/Mn_1@qHP\text{-}C_{60}) = |S(Mn_1@qHP\text{-}C_{60}) - S(O_2)|, |S(Mn_1@qHP\text{-}C_{60}) - S(O_2)| + 1, \ldots, |S(Mn_1@qHP\text{-}C_{60}) + S(O_2)|$, where $S(Mn_1@qHP\text{-}C_{60})$ and $S(O_2)$ are the spin quantum numbers of the Mn_1@qHP-C_{60} system and a freestanding O_2 molecule, respectively. The changes of the magnetic moments (ΔM) upon O_2 adsorption are presented in Fig. 2(b). Specifically, O_2 undergoes a spin-triplet to spin-singlet transition, with its initial 2.0 μ_B MM totally quenched to nearly zero, -0.04 μ_B; hence, the ΔM amounts to 2.04 μ_B. Consequently, as restricted by the aforementioned spin selection [37], such a ΔM should be accommodated by the supporting Mn_1@qHP-C_{60} system. Notably, the ΔM of the

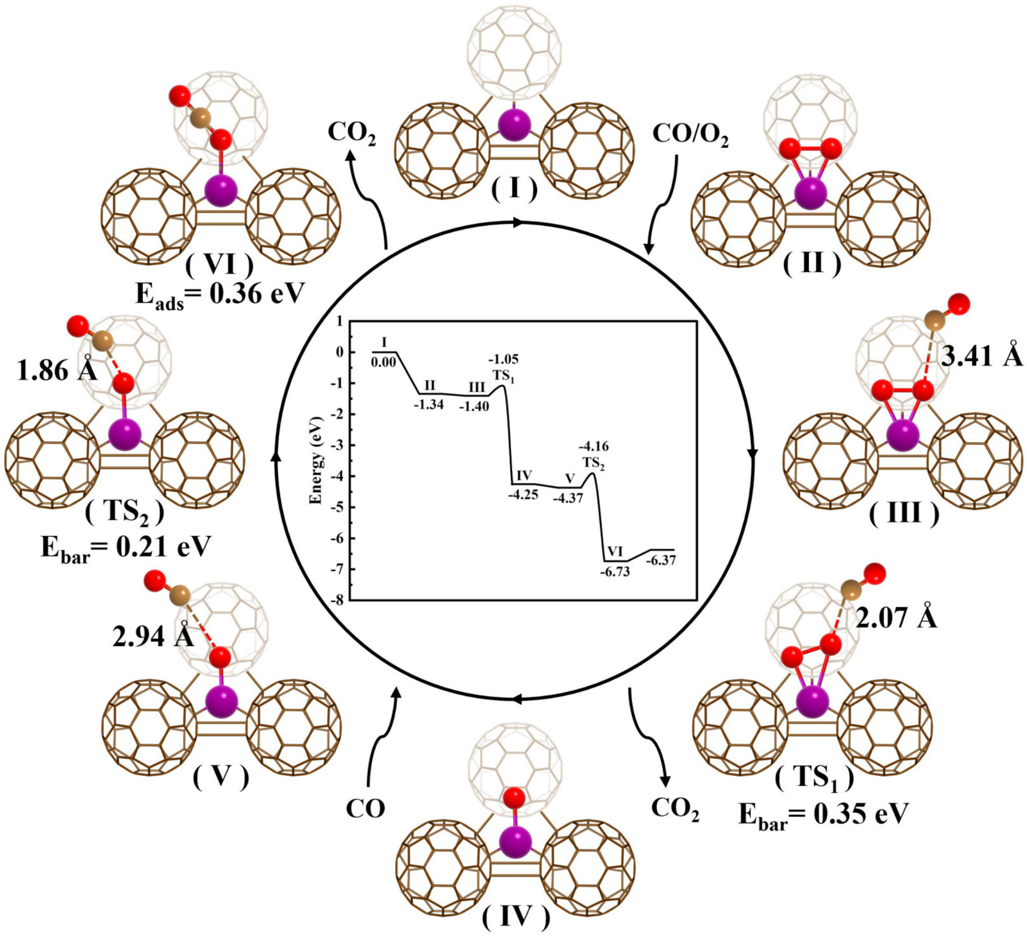

FIG. 3. Schematic illustration of E–R mechanism cycle diagram for CO oxidation on Mn_1@qHP-C_{60}.

hosting reactive-Mn single atom is negligible, ~0.02 μ_B. Contrastingly, the *p*-block qHP-C_{60} accommodates all the MM reduction of O_2 and Mn atoms, via modifying its own MM by 2.06 μ_B, as also supported in Fig. 2(b). These findings reveal that the *p*-block elemental qHP-C_{60} not only donates most of the charge transfer, but also functions as a spin sponge, exerting dominance over the spin selection in O_2 activation.

To further illustrate the underlying mechanism for O_2 activation, we present the local projected electronic density of states (DOS) for the cases of before and after O_2 adsorption, as shown in Figs. 2(c) and 2(d). Note that the pristine qHP-C_{60} network exhibits a semiconducting feature; see Fig. 1(b). However, in the initial state where O_2 molecule is positioned far (~7 Å) away from Mn_1@qHP-C_{60}, the charge transfer from the supported Mn induces significant contributions to the local DOS around the Fermi energy (E_F) of the Mn_1@qHP-C_{60} complex [Fig. 2(c)]. Furthermore, Mn hybridizes with the underlying qHP-C_{60} approximately 0.6 eV below the E_F in spin-minority states. This rationalizes the crucial role played by the underlying qHP-C_{60} in both charge transfer and spin interactions for O_2 activation through the Mn single-atomic reactive site. Note that in such an initial state, the antibonding orbital of the O_2 molecule exhibits a spin-minority feature right above the E_F. Upon adsorption, the spin-majority and spin-minority orbitals of O_2 species hybridize strongly with the Mn single atom and the qHP-C_{60} support within the energy ranges of [-3.5, -3.0 eV] and [-2.7, -2.0 eV], respectively. Simultaneously, the unoccupied spin-minority DOS of O_2 is significantly reduced, with both spin-majority and spin-minority DOS peaks merging just below the E_F. More specifically, the spin-minority DOS of qHP-C_{60} right below the E_F vanishes [see Fig. 2(d)], rationalizing the functionalities of the qHP-C_{60} in serving as both charge donor and spin acceptor.

Now, using Mn_1@qHP-C_{60} system as a typical example, we explore the energetics and kinetic processes of CO oxidation. Due to the larger E_{ads} of O_2 (1.34 eV) than that of CO (0.64 eV) on Mn_1@qHP-C_{60} (structure I), the Eley-Rideal (E-R) mechanism [61] is preferentially considered, as schematically shown in Fig. 3. In such a process, the O_2 molecule is initially adsorbed (structure II), followed by a direct attack from an incoming CO. The initial state (III) is characterized by a CO distance of about 3.41 Å away from the adsorbed O_2 species. Then, the incoming CO molecule can readily react with the oxygen atom of the activated O_2 molecule, overcoming a relatively low energy barrier (E_{bar}) of 0.35 eV in the first transition state (TS_1). Subsequently, a CO_2 molecule can be smoothly released, as shown in the first final state (IV). Further calculations indicate that the remaining O atom on the Mn active site can be easily attacked by the second entering CO molecule, with an E_{bar} of 0.21 eV in the second transition state (TS_2). Finally, the

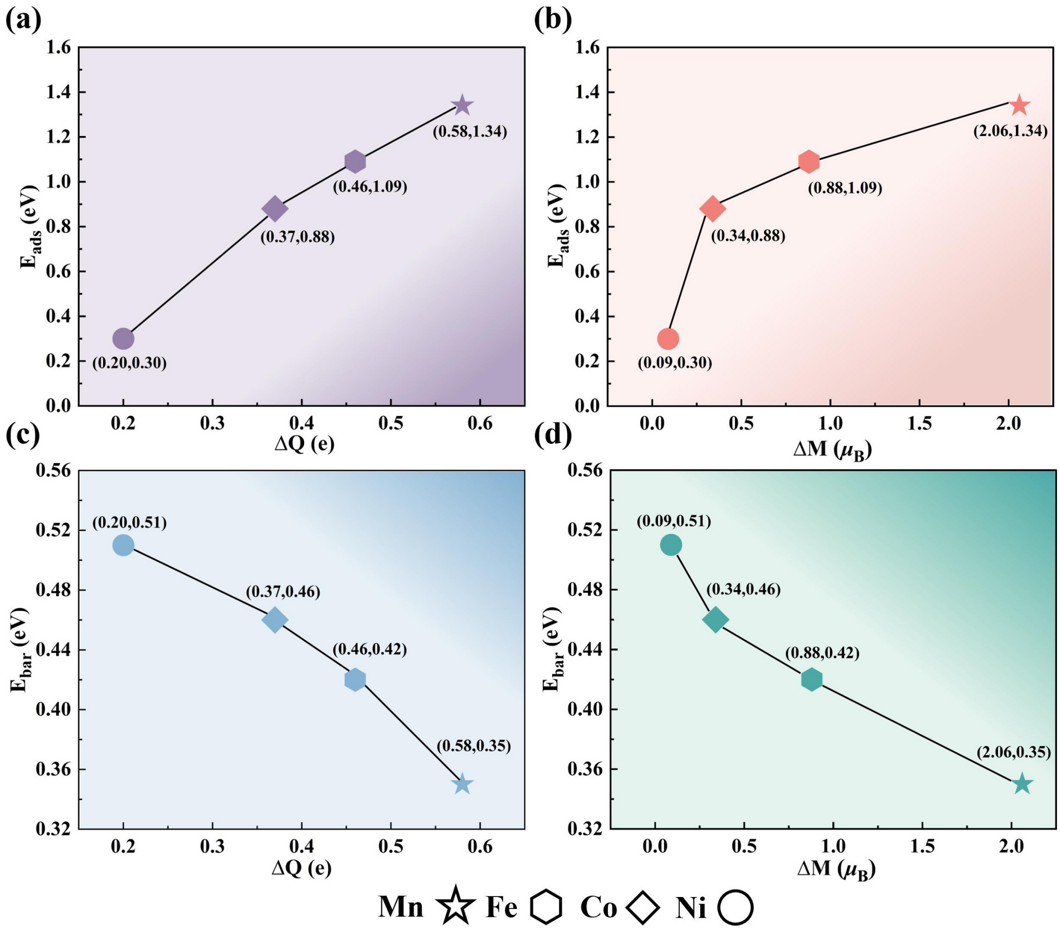

FIG. 4. Adsorption energy (E_{ads}) of O_2 molecule and reaction energy barrier (E_{bar}) of the first round of CO oxidation as a function of (a), (c) charge donation; (b), (d) spin accommodation by qHP-C_{60}, for the cases of TM_1@qHP-C_{60} (TM = Mn, Fe, Co, and Ni), respectively.

second CO_2 molecule can be smoothly released by overcoming a desorption energy of 0.36 eV. Furthermore, the Langmuir-Hinshelwood (L-H) process [62] is detailed in Sec. II of the Supplemental Material, Fig. S6 [54].

Moreover, based on an Arrhenius-type activation process, the reaction rates of both E-R and L-H processes of the CO oxidation on Mn_1@qHP-C_{60} have been calculated: 8.95×10^6 and $2.65\times10^3\ s^{-1}$ for the former and latter, respectively. These findings suggest that the CO oxidation preferentially proceeds via the E-R mechanism. Note also that the CO oxidation rate via the E-R process is about 15 orders of amplitude higher than the nucleation rate of the Mn single atoms (with a diffusion E_{bar} of 1.27 eV). Collectively, these findings strongly suggest the high performance of the present Mn_1@qHP-C_{60} SAC complex.

We continue to address the charge transfer and the MM evolution in the key steps of CO oxidation on Mn_1@qHP-C_{60} via the E-R process (see Sec. II of the Supplemental Material, Fig. S7 [54]). The initial structure I presented in Fig. 3 is taken as the reference point. In step II, where the O_2 is adsorbed on the single Mn site and undergoes a charge accumulation of ~0.84 $|e|$. Remarkably, about two-thirds of this charge is observed to be donated back from the qHP-C_{60} network. Similarly, in the TS_1 (TS_2), the qHP-C_{60} support contributes 0.64 (0.64) $|e|$ to the reactants of O_2 and CO species; nevertheless, the Mn single atom provides merely 0.27 (0.18) $|e|$. Considering that in structure I the Mn atoms donate about 1.06 $|e|$ to the qHP-C_{60} support, it can be inferred that more than half of this charge is returned to the reactants. This conclusion is further confirmed in O_2 activation and CO oxidation on three other typical TM_1@qHP-C_{60} systems (TM = Fe, Co, and Ni), as discussed shortly. These findings unambiguously demonstrate the distinctive functionality of the p-block elemental qHP-C_{60} in serving as a charge reservoir for O_2 activation and CO oxidation. Alternatively, regarding the spin aspect (see Sec. II of the Supplemental Material, Fig. S7 [54]), the change of the spin magnetic moments of O_2 molecule is predominantly accommodated by the supporting qHP-C_{60} network, rather than the Mn single-atom reactive site. Collectively, these observations convincingly demonstrate that qHP-C_{60} not only serves as a charge reservoir, but also functions as a spin sponge, obeying the spin selection during the process of spin-triplet O_2 activation and CO oxidation.

Close to the end, to further demonstrate the broad applicability of the present 2D qHP-C_{60} network in serving as both charge and spin reservoir in Mn_1@qHP-C_{60} complex, we conducted a concise comparative study of CO oxidation on three other typical TM_1@qHP-C_{60} systems (TM = Fe, Co, and Ni). And, a robust correlation between ΔQ (ΔM) contributed by the qHP-C_{60} and the O_2 activation is established: the larger the ΔQ (ΔM), the larger the E_{ads} of O_2, as demonstrated

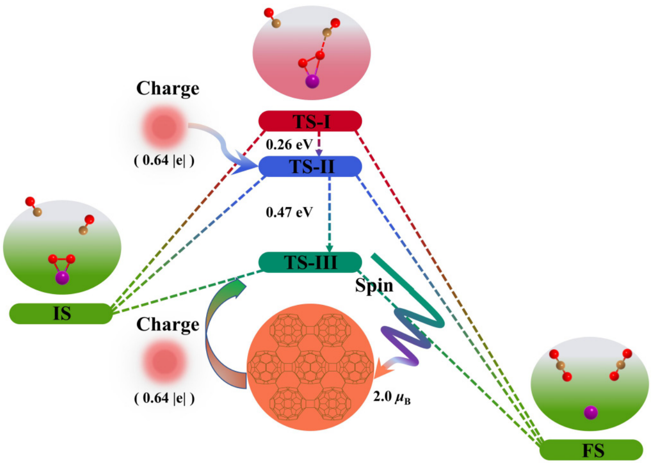

FIG. 5. Schematic show the quantitative contributions of charge transfer and spin accommodation of the qHP-C_{60} network substrate in reducing the value of the E_{bar} for CO oxidation on the Mn single-atom reactive site.

in Figs. 4(a) and 4(b) and detailed in Sec. II of the Supplemental Material, Fig. S8 [54]. Additionally, the optimum CO oxidation processes on TM_1@qHP-C_{60} (TM = Fe, Co, and Ni) systems are depicted in Sec. II of the Supplemental Material, Figs. S9–S11 [54]. Importantly, in the first round of CO oxidation accompanied with O_2 dissociation, for the four TM_1@qHP-C_{60} (TM = Mn, Fe, Co, and Ni) catalysts, a clear quasilinear correlation between the calculated E_{bar} and ΔQ (ΔM) of the qHP-C_{60} component is established, i.e., the larger the ΔQ (ΔM), the lower the E_{bar} [see Figs. 4(c) and 4(d)]. Moreover, the calculated E_{bar} in the minimum-energy pathways for CO oxidation on the four current TM_1@qHP-C_{60} structures fall within the range of $0.36 \sim 0.51$ eV, which are either lower than or comparable to those observed in various high-performance single atomic-scale noble-metal catalysts [63,64]. However, such a specific strong correlation between the calculated E_{bar} and ΔM (ΔQ) contributed by the TM single atoms is not observed (see Sec. II of the Supplemental Material, Fig. S8 [54]).

To this end, we perform delicate comparisons to quantitatively identify the importance of the spin sponge functionality of the qHP-C_{60} in CO oxidation. Our computational results demonstrate that for O_2 activation and CO oxidation on an isolated gas-phase Mn single atom, the calculated rate-limiting E_{bar} is significantly increased to 1.09 eV (see Fig. 5, TS-I and details in Sec. II of the Supplemental Material, Fig. S12 [54]). Moreover, as a first-order approximation, the introduction of an additional 0.64 $|e|$ (equivalent to the ΔQ contributed by the qHP-C_{60} support in TS_1; see Sec. II of the Supplemental Material, Fig. S7(a) [54]) into the simulation cell consisting of the Mn single atom and O_2/CO reactants yields a calculated E_{bar} as high as 0.83 eV; see TS-II in Fig. 5, as calculated by the self-consistent potential correction method [65]. Typically, the same quantity of pure charge transfer merely lowers the E_{bar} by 0.26 eV. In contrast, the spin accommodation of the O_2 molecule by the 2D qHP-C_{60} network further significantly lowers the E_{bar} by 0.47 eV, approximately twice as much as that of a pure charge transfer; see TS-III in Fig. 5. These findings convincingly demonstrate the crucial role of the spin sponge of the *p*-block 2D qHP-C_{60} network in facilitating highly efficient O_2 activation and CO oxidation.

IV. CONCLUSIONS

In conclusion, utilizing state-of-the-art first-principles calculations, we demonstrate that the recently fabricated class of 2D carbon material, covalent-bond-linked monolayer C_{60} *p*-block elemental network, can serve as an ideal platform in stabilizing transition metals (Mn, Fe, Co, and Ni) into dispersive single atoms, and functions as amazing spin sponge to effectively activate spin-triplet O_2 molecule. Also importantly, we quantitatively figure out that the spin aspect plays a vital role approximately twice as significant as that of pure charge transfer in reducing the activation barrier for O_2 activation and CO oxidation. The importance of spin degree of freedom of the *p*-block elemental C_{60} network is quantitatively revealed in catalysis. These findings could be expected to direct appealing application territory of the two-dimensional C_{60} network in spin-catalysis and related fields.

ACKNOWLEDGMENTS

This work was supported by the National Natural Science Foundation of China (Grants No. 12174349, No. U23A2072, and No. 12074345). The calculations were performed on the National Supercomputing Center in Zhengzhou, Zhengzhou University, Henan.

[1] A. Hirsch, The era of carbon allotropes, Nat. Mater. **9**, 868 (2010).
[2] H. W. Kroto, J. R. Heath, S. C. O'Brien, R. F. Curl, and R. E. Smalley, C_{60}: Buckminsterfullerene, Nature (London) **318**, 162 (1985).
[3] S. Iijima, Helical microtubules of graphitic carbon, Nature (London) **354**, 56 (1991).
[4] K. S. Novoselov, A. K. Geim, S. V. Morozov, D. Jiang, Y. Zhang, S. V. Dubonos, I. V. Grigorieva, and A. A. Firsov, Electric field effect in atomically thin carbon films, Science **306**, 666 (2004).
[5] F. P. Bundy, H. T. Hall, H. M. Strong, and R. H. Wentorfjun, Man-made diamonds, Nature (London) **176**, 51 (1955).
[6] V. Georgakilas, J. N. Tiwari, K. C. Kemp, J. A. Perman, A. B. Bourlinos, K. S. Kim, and R. Zboril, Noncovalent functionalization of graphene and graphene oxide for energy materials, biosensing, catalytic, and biomedical applications, Chem. Rev. **116**, 5464 (2016).
[7] X. Chang, Y. Xu, and M. von Delius, Recent advances in supramolecular fullerene chemistry, Chem. Soc. Rev. **53**, 47 (2024).
[8] M. Feng, J. Zhao, and H. Petek, Atomlike, hollow-core-bound molecular orbitals of C_{60}, Science **320**, 359 (2008).
[9] G. Yu, J. Gao, J. C. Hummelen, F. Wudl, and A. J. Heeger, Polymer photovoltaic cells: Enhanced efficiencies via a network

of internal donor-acceptor heterojunctions, Science **270**, 1789 (1995).

[10] L. Jia, X. Ma, W. Xiang, X. Jiang, H. Ding, X. Li, Y. Shang, J. Zhu, Z. Li, Y. Qiu, M. Chen, J. Chen, and S. Yang, Lowering the dielectric mismatch for efficient inverted perovskite solar cells through incorporating cyano-functionalized fullerene additive, Sci. China Mater. **66**, 2146 (2023).

[11] C. Joachim, J. K. Gimzewski, R. R. Schlittler, and C. Chavy, Electronic transparence of a single C_{60} molecule, Phys. Rev. Lett. **74**, 2102 (1995).

[12] H. Park, J. Park, A. K. L. Lim, E. H. Anderson, A. P. Alivisatos, and P. L. McEuen, Nanomechanical oscillations in a single-C_{60} transistor, Nature (London) **407**, 57 (2000).

[13] J. Taylor, H. Guo, and J. Wang, Ab initio modeling of open systems: Charge transfer, electron conduction, and molecular switching of a C_{60} device, Phys. Rev. B **63**, 121104(R) (2001).

[14] A. R. Champagne, A. N. Pasupathy, and D. C. Ralph, Mechanically adjustable and electrically gated single-molecule transistors, Nano Lett. **5**, 305 (2005).

[15] H. Nie, C. Zhao, Z. Shi, C. Jia, and X. Guo, Single-molecule fullerenes: Current stage and perspective, ACS Mater. Lett. **4**, 1037 (2022).

[16] H. Imahori and Y. Sakata, Donor-linked fullerenes: Photoinduced electron transfer and its potential application, Adv. Mater. **9**, 537 (1997).

[17] Z. Xu, Y. Wang, Y. Li, Y. Wang, B. Peng, K. Davey, L. Sun, G. Li, S. Zhang, and Z. Guo, C_{60} and derivatives boost electrocatalysis and photocatalysis: Electron buffers to heterojunctions, Adv. Energy Mater. **13**, 2302438 (2023).

[18] Q. Xie, E. Perez-Cordero, and L. Echegoyen, Electrochemical detection of C_{60}^{6-} and C_{70}^{6-}: Enhanced stability of fullerides in solution, J. Am. Chem. Soc. **114**, 3978 (1992).

[19] L. Echegoyen and L. E. Echegoyen, Electrochemistry of fullerenes and their derivatives, Acc. Chem. Res. **31**, 593 (1998).

[20] J. Zheng, L. Huang, C.-H. Cui, Z.-C. Chen, X.-F. Liu, X. Duan, X.-Y. Cao, T.-Z. Yang, H. Zhu, K. Shi, P. Du, S.-W. Ying, C.-F. Zhu, Y.-G. Yao, G.-C. Guo, Y. Yuan, S.-Y. Xie, and L.-S. Zheng, Ambient-pressure synthesis of ethylene glycol catalyzed by C_{60}-buffered Cu/SiO_2, Science **376**, 288 (2022).

[21] X.-D. Xiang, J. G. Hou, G. Briceño, W. A. Vareka, R. Mostovoy, A. Zettl, V. H. Crespi, and M. L. Cohen, Synthesis and electronic transport of single crystal K_3C_{60}, Science **256**, 1190 (1992).

[22] G.-L. Hou, T. Yang, M. Li, J. Vanbuel, O. V. Lushchikova, P. Ferrari, J. M. Bakker, and E. Janssens, Water splitting by C_{60}-supported vanadium single atoms, Angew. Chem. Int. Ed. **60**, 27095 (2021).

[23] Y. Li, T. Xu, Q. Huang, L. Zhu, Y. Yan, P. Peng, and F.-F. Li, C_{60} Fullerenol to stabilize and activate Ru nanoparticles for highly efficient hydrogen evolution reaction in alkaline media, ACS Catal. **13**, 7597 (2023).

[24] R. Zhang, Y. Li, X. Zhou, A. Yu, Q. Huang, T. Xu, L. Zhu, P. Peng, S. Song, L. Echegoyen, and F.-F. Li, Single-atomic platinum on fullerene C_{60} surfaces for accelerated alkaline hydrogen evolution, Nat. Commun. **14**, 2460 (2023).

[25] L. Hou, X. Cui, B. Guan, S. Wang, R. Li, Y. Liu, D. Zhu, and J. Zheng, Synthesis of a monolayer fullerene network, Nature (London) **606**, 507 (2022).

[26] E. Meirzadeh, A. M. Evans, M. Rezaee, M. Milich, C. J. Dionne, T. P. Darlington, S. T. Bao, A. K. Bartholomew, T. Handa, D. J. Rizzo, R. A. Wiscons, M. Reza, A. Zangiabadi, N. Fardian-Melamed, A. C. Crowther, P. J. Schuck, D. N. Basov, X. Zhu, A. Giri, P. E. Hopkins *et al.*, A few-layer covalent network of fullerenes, Nature (London) **613**, 71 (2023).

[27] F. Pan, K. Ni, T. Xu, H. Chen, Y. Wang, K. Gong, C. Liu, X. Li, M.-L. Lin, S. Li, X. Wang, W. Yan, W. Yin, P.-H. Tan, L. Sun, D. Yu, R. S. Ruoff, and Y. Zhu, Long-range ordered porous carbons produced from C_{60}, Nature (London) **614**, 95 (2023).

[28] L. Yu, J. Xu, B. Peng, G. Qin, and G. Su, Anisotropic optical, mechanical, and thermoelectric properties of two-dimensional fullerene networks, J. Phys. Chem. Lett. **13**, 11622 (2022).

[29] B. Peng, Monolayer fullerene networks as photocatalysts for overall water splitting, J. Am. Chem. Soc. **144**, 19921 (2022).

[30] Y. Tong, H. Liu, S. Dai, and D.-E. Jiang, Monolayer fullerene membranes for hydrogen separation, Nano Lett. **23**, 7470 (2023).

[31] T. Wang, L. Zhang, J. Wu, M. Chen, S. Yang, Y. Lu, and P. Du, Few-layer fullerene network for photocatalytic pure water splitting into H_2 and H_2O_2, Angew. Chem. Int. Ed. **62**, e202311352 (2023).

[32] Q.-K. Li, X.-F. Li, G. Zhang, and J. Jiang, Cooperative spin transition of monodispersed FeN_3 sites within graphene induced by CO adsorption, J. Am. Chem. Soc. **140**, 15149 (2018).

[33] Z. Li, Z. Wang, S. Xi, X. Zhao, T. Sun, J. Li, W. Yu, H. Xu, T. S. Herng, X. Hai, P. Lyu, M. Zhao, S. J. Pennycook, J. Ding, H. Xiao, and J. Lu, Tuning the spin density of cobalt single-atom catalysts for efficient oxygen evolution, ACS Nano **15**, 7105 (2021).

[34] G. Yang, J. Zhu, P. Yuan, Y. Hu, G. Qu, B.-A. Lu, X. Xue, H. Yin, W. Cheng, J. Cheng, W. Xu, J. Li, J. Hu, S. Mu, and J.-N. Zhang, Regulating Fe-spin state by atomically dispersed Mn-N in Fe-N-C catalysts with high oxygen reduction activity, Nat. Commun. **12**, 1734 (2021).

[35] E. Wigner and E. E. Witmer, Über die struktur der zweiatomigen molekelspektren nach der quantenmechanik, Z. Med. Phys. **51**, 859 (1928).

[36] C. Carbogno, J. Behler, A. Groß, and K. Reuter, Fingerprints for spin-selection rules in the interaction dynamics of O_2 at Al(111), Phys. Rev. Lett. **101**, 096104 (2008).

[37] L. Zhang, X. Ren, X. Zhao, Y. Zhu, R. Pang, P. Cui, Y. Jia, S. Li, and Z. Zhang, Synergetic charge transfer and spin selection in CO oxidation at neighboring magnetic single-atom catalyst sites, Nano Lett. **22**, 3744 (2022).

[38] X. Ren, T. Wu, Y. Sun, Y. Li, G. Xian, X. Liu, C. Shen, J. Gracia, H.-J. Gao, H. Yang, and Z. J. Xu, Spin-polarized oxygen evolution reaction under magnetic field, Nat. Commun. **12**, 2608 (2021).

[39] A. Cao, V. J. Bukas, V. Shadravan, Z. Wang, H. Li, J. Kibsgaard, I. Chorkendorff, and J. K. Nørskov, A spin promotion effect in catalytic ammonia synthesis, Nat. Commun. **13**, 2382 (2022).

[40] C.-C. Lin, T.-R. Liu, S.-R. Lin, K. M. Boopathi, C.-H. Chiang, W.-Y. Tzeng, W.-H. C. Chien, H.-S. Hsu, C.-W. Luo, H.-Y. Tsai, H.-A. Chen, P.-C. Kuo, J. Shiue, J.-W. Chiou, W.-F. Pong, C.-C. Chen, and C.-W. Chen, Spin-polarized photocatalytic CO_2 reduction of Mn-doped perovskite nanoplates, J. Am. Chem. Soc. **144**, 15718 (2022).

[41] W. Kohn and L. J. Sham, Self-consistent equations including exchange and correlation effects, Phys. Rev. **140**, A1133 (1965).

[42] G. Kresse and J. Furthmüller, Efficient iterative schemes for ab initio total-energy calculations using a plane-wave basis set, Phys. Rev. B **54**, 11169 (1996).

[43] G. Kresse and J. Furthmüller, Efficiency of ab-initio total energy calculations for metals and semiconductors using a plane-wave basis set, Comput. Mater. Sci. **6**, 15 (1996).

[44] P. E. Blöchl, Projector augmented-wave method, Phys. Rev. B **50**, 17953 (1994).

[45] G. Kresse and D. Joubert, From ultrasoft pseudopotentials to the projector augmented-wave method, Phys. Rev. B **59**, 1758 (1999).

[46] B. Hammer, L. B. Hansen, and J. K. Nørskov, Improved adsorption energetics within density-functional theory using revised Perdew-Burke-Ernzerhof functionals, Phys. Rev. B **59**, 7413 (1999).

[47] A. I. Liechtenstein, V. I. Anisimov, and J. Zaanen, Density-functional theory and strong interactions: Orbital ordering in Mott-Hubbard insulators, Phys. Rev. B **52**, R5467(R) (1995).

[48] H. Xu, D. Cheng, D. Cao, and X. C. Zeng, A universal principle for a rational design of single-atom electrocatalysts, Nat. Catal. **1**, 339 (2018).

[49] S. Grimme, J. Antony, S. Ehrlich, and H. Krieg, A consistent and accurate ab initio parametrization of density functional dispersion correction (DFT-D) for the 94 elements H-Pu, J. Chem. Phys. **132**, 154104 (2010).

[50] S. Grimme, S. Ehrlich, and L. Goerigk, Effect of the damping function in dispersion corrected density functional theory, J. Comput. Chem. **32**, 1456 (2011).

[51] G. Henkelman and H. Jónsson, Improved tangent estimate in the nudged elastic band method for finding minimum energy paths and saddle points, J. Chem. Phys. **113**, 9978 (2000).

[52] G. Henkelman, B. P. Uberuaga, and H. Jónsson, A climbing image nudged elastic band method for finding saddle points and minimum energy paths, J. Chem. Phys. **113**, 9901 (2000).

[53] J. Heyd, G. E. Scuseria, and M. Ernzerhof, Hybrid functionals based on a screened Coulomb potential, J. Chem. Phys. **118**, 8207 (2003).

[54] See Supplemental Material at http://link.aps.org/supplemental/10.1103/PhysRevB.110.125405 for the adsorption sites, binding energy, thermodynamic stability, the configurations of four Mn atoms deposited on qHP-C_{60}, relative energies with different spin configurations, adsorption energies of O_2 and CO molecules on the TM1@qHP-C_{60} (TM = Mn, Fe, Co, and Ni), reaction mechanism for CO oxidation, and the charge transfer and spin magnetic moment change in the step of O_2 adsorption (coadsorption) on the TM1@qHP-C_{60} systems.

[55] L. A. Ribeiro, M. L. Pereira, W. F. Giozza, R. M. Tromer, and D. S. Galvão, Thermal stability and fracture patterns of a recently synthesized monolayer fullerene network: A reactive molecular dynamics study, Chem. Phys. Lett. **807**, 140075 (2022).

[56] S.-J. Dixon-Warren, E. T. Jensen, and J. C. Polanyi, Direct evidence for charge-transfer photodissociation at a metal surface: CCl_4/Ag(111), Phys. Rev. Lett. **67**, 2395 (1991).

[57] N. Mulakaluri, R. Pentcheva, M. Wieland, W. Moritz, and M. Scheffler, Partial dissociation of water on Fe_3O_4 (001): Adsorbate induced charge and orbital order, Phys. Rev. Lett. **103**, 176102 (2009).

[58] J. Behler, B. Delley, S. Lorenz, K. Reuter, and M. Scheffler, Dissociation of O_2 at Al(111): The role of spin selection rules, Phys. Rev. Lett. **94**, 036104 (2005).

[59] A. C. Reber, S. N. Khanna, P. J. Roach, W. H. Woodward, and A. W. Castleman, Spin accommodation and reactivity of aluminum based clusters with O_2, J. Am. Chem. Soc. **129**, 16098 (2007).

[60] Y. Sun, S. Sun, H. Yang, S. Xi, J. Gracia, and Z. J. Xu, Spin-related electron transfer and orbital interactions in oxygen electrocatalysis, Adv. Mater. **32**, 2003297 (2020).

[61] E. K. Rideal, A note on a simple molecular mechanism for heterogeneous catalytic reactions, Math. Proc. Cambridge Philos. Soc. **35**, 130 (1939).

[62] I. Langmuir, Part II.—"Heterogeneous reactions." Chemical reactions on surfaces, Trans. Faraday Soc. **17**, 607 (1922).

[63] W. E. Kaden, T. Wu, W. A. Kunkel, and S. L. Anderson, Electronic structure controls reactivity of size-selected Pd clusters adsorbed on TiO_2 surfaces, Science **326**, 826 (2009).

[64] Y. Ren, Y. Tang, L. Zhang, X. Liu, L. Li, S. Miao, D. Sheng Su, A. Wang, J. Li, and T. Zhang, Unraveling the coordination structure-performance relationship in Pt_1/Fe_2O_3 single-atom catalyst, Nat. Commun. **10**, 4500 (2019).

[65] M. Chagas da Silva, M. Lorke, B. Aradi, M. Farzalipour Tabriz, T. Frauenheim, A. Rubio, D. Rocca, and P. Deák, Self-consistent potential correction for charged periodic systems, Phys. Rev. Lett. **126**, 076401 (2021).